nature communications

Article

https://doi.org/10.1038/s41467-024-52125-8

Direct observation of ion cyclotron damping of turbulence in Earth's magnetosheath plasma

Received: 26 January 2023

Accepted: 26 August 2024

A. S. Afshari[1], G. G. Howes[1], J. R. Shuster[2], K. G. Klein[3], D. McGinnis[1], M. M. Martinović[3], S. A. Boardsen[4,5], C. R. Brown[1], R. Huang[1], D. P. Hartley[1] & C. A. Kletzing[1]

Plasma turbulence plays a key role in space and astrophysical plasma systems, enabling the energy of magnetic fields and plasma flows to be transported to particle kinetic scales at which the turbulence dissipates and heats the plasma. Identifying the physical mechanisms responsible for the dissipation of the turbulent energy is a critical step in developing the predictive capability for the turbulent heating needed by global models. In this work, spacecraft measurements of the electromagnetic fields and ion velocity distributions by the Magnetospheric Multiscale (MMS) mission are used to generate velocity-space signatures that identify ion cyclotron damping in Earth's turbulent magnetosheath, in agreement with analytical modeling. Furthermore, the rate of ion energization is directly quantified and combined with a previous analysis of the electron energization to identify the dominant channels of turbulent dissipation and determine the partitioning of energy among species in this interval.

Turbulence plays an essential role in space and astrophysical plasmas by mediating the transport of the energy in large-scale magnetic fields and plasma flows down to smaller scales, where poorly constrained physical mechanisms damp the turbulent fluctuations and thereby energize the plasma particles, yielding either heating of the plasma species or acceleration of particles[1]. Predicting the heating or acceleration of the different plasma species by turbulence, based on the observable turbulence and plasma parameters at large scales, is recognized as a grand challenge problem in heliophysics[2], critical to ongoing efforts to globally model[3–5] the flow of energy from the Sun through the interplanetary medium to the Earth, other planets, and on to the boundary of the heliosphere with the surrounding interstellar medium[6]. Such predictive models of turbulent plasma heating[7,8] are also critical for the interpretation of remote astronomical observations of emissions from black hole accretion disks, such as the groundbreaking observations by the Event Horizon Telescope of the supermassive black holes at the center of M87[9] and at Sagittarius A* in the Milky Way[10], where alternative turbulent heating prescriptions yield drastically different predictions for the emitted radiation[11].

Identifying the physical mechanisms governing the dissipation of the turbulence and quantifying the resulting partitioning of energy among the plasma species are two essential steps in achieving the long-term goal of developing a predictive capability for plasma turbulence. Physical mechanisms proposed to govern the dissipation of turbulence in weakly collisional space plasmas include resonant wave-particle interactions (e.g., Landau damping[12,13], transit-time damping[14], cyclotron damping[15]), non-resonant wave-particle interactions (e.g., stochastic ion heating[16–18], magnetic pumping[19],"viscous" heating mediated by temperature anisotropy instabilities[20]), and dissipation in coherent structures (e.g., magnetic reconnection in current sheets[21–24]).

Previous studies have used proton and helium temperature anisotropy measurements in the solar wind as a function of the plasma parameters and the differential ion flow to argue indirectly that ion cyclotron damping leads to enhanced perpendicular ion temperatures

---

[1]Department of Physics and Astronomy, University of Iowa, Iowa City, IA 52242, USA. [2]Space Science Center, Institute for the Study of Earth, Oceans, and Space and University of New Hampshire, Durham, NH 03824, USA. [3]University of Arizona, Department of Planetary Sciences, Lunar and Planetary Laboratory, 1629 E University Blvd, Tucson, AZ 85721, USA. [4]NASA Goddard Space Flight Center, Greenbelt, MD, USA. [5]Goddard Planetary Heliophysics Institute, University of Maryland, Baltimore, MD, USA. e-mail: arya-afshari@uiowa.edu

in the inner heliosphere[25,26], though an alternative analysis suggests that ion stochastic heating may also lead to similar observational signatures[16]. Another study used the Flux Angle operation mode on the Solar Probe Cup[27] of the Parker Solar Probe (PSP)[28,29] to measure the correlation between fluctuations of the perpendicular electric field and the fluctuations within a narrow range of the proton velocity distribution[30], showing evidence of energy transfer between ion cyclotron waves (ICWs) and the protons. More recently, PSP observations in the inner heliosphere at 30 solar radii showed ion velocity distributions elongated anisotropically in the direction perpendicular to the magnetic field, with contours consistent with the expectations for quasilinear diffusion due to a spectrum of parallel ICWs; using the observed spectrum of left-handed fluctuations, an ion cyclotron heating rate was estimated by applying the quasilinear diffusion operator to the measured velocity distribution[31].

Here we apply the field-particle correlation (FPC) technique[32–35] to spacecraft observations from the Magnetospheric Multiscale (MMS) mission[36] to provide direct measurements of ion cyclotron damping in the Earth's turbulent magnetosheath plasma and to determine the resulting rate of ion energization. By combining perpendicular electric field and ion velocity distribution measurements from the MMS spacecraft, we generate velocity-space signatures that identify ion cyclotron damping of the ICWs observed within the turbulent spectrum. Furthermore, these measurements enable us to compute the rate of work done by the perpendicular electric field on the ions. In combination with a previous analysis of electron Landau damping during the same interval[37], we show that we have identified all significant channels of turbulent energy dissipation at small scales, observationally quantifying the partitioning of turbulent energy between ions and electrons.

Results

Event overview and evidence of ion cyclotron waves

We analyze a 77-second interval of burst-mode data from the MMS1 spacecraft starting at 07:24:28 on 12 January 2016. At this time, the spacecraft probed the Earth's magnetosheath—the region of shocked solar wind bounded by the bow shock and the magnetopause—at a position near the dawnward side of the sub-solar point close to the magnetopause, where the turbulent cascade is generally found to be well developed[38]. Previous examination of this interval in Afshari et al. (Interval 02 of that study) identified that electron Landau damping accounted for approximately 7.5% of the dissipation of the estimated turbulent cascade rate[37].

Here we use magnetic field data sampled at 128 Hz from the Fluxgate Magnetometers (FGM)[39], electric field data sampled at 8192 Hz from the Electric Field Double Probes (EDP)[40,41], and full sky measurements of the ion velocity distribution functions (iVDFs) at a cadence of 150 ms from the Fast Plasma Investigation (FPI) Dual Ion Spectrometers (DIS)[42]. This event was selected due to having relatively constant plasma parameters over the duration of the interval: magnetic field magnitude $|\mathbf{B}_0| = 48 \pm 5$ nT, ion number density $n_i = 8.6 \pm 0.6$ cm^{-3}, perpendicular and parallel ion temperatures $T_{\perp i} = 614 \pm 30$ eV and $T_{\parallel i} = 253 \pm 14$ eV yielding an effective isotropic ion temperature $T_i = (2T_{\perp i} + T_{\parallel i})/3 = 494 \pm 22$ eV, perpendicular and parallel electron temperatures $T_{\perp e} = 36 \pm 2$ eV and $T_{\parallel e} = 37 \pm 4$ eV yielding an effective isotropic electron temperature $T_e = (2T_{\perp e} + T_{\parallel e})/3 = 37 \pm 2$ eV, perpendicular and parallel ion thermal speed $v_{\perp ti} = (2T_{\perp i}/m_i)^{1/2} = 343 \pm 8$ km/s and $v_{\parallel ti} = (2T_{\parallel i}/m_i)^{1/2} = 220 \pm 6$ km/s, Alfvén speed $v_A = B_0/(\mu_0 m_i n_i)^{1/2} = 355 \pm 21$ km/s, parallel ion plasma beta $\beta_{\parallel i} = v_{\parallel ti}^2/v_A^2 = 2\mu_0 n_i T_i/B^2 = 0.383 \pm 0.058$, linear ion (proton) cyclotron frequency $f_{ci} = q_i B_0/(2\pi m_i) = 0.73 \pm 0.02$ Hz, and ion bulk flow speed $|\mathbf{U}_{0i}| = 122 \pm 38$ km/s. Here the standard deviation quantifies the variation in the parameters; the parallel and perpendicular directions are with respect to the mean magnetic field $\mathbf{B}_0$. The relevant wave forms are shown in Fig. 1, with the 77-second interval denoted by the dashed vertical lines.

The magnetic field energy spectrum over 07:00–08:00, calculated using a Morlet wavelet transform[43,44] and shown in Fig. 2a, exhibits excess power predominantly in the time range 07:15–07:38, over the frequency range 0.2Hz $\lesssim f \lesssim$ 0.5 Hz. The dimensionless trace magnetic and electric spectra, shown in Fig. 2b, exhibit a spectral index

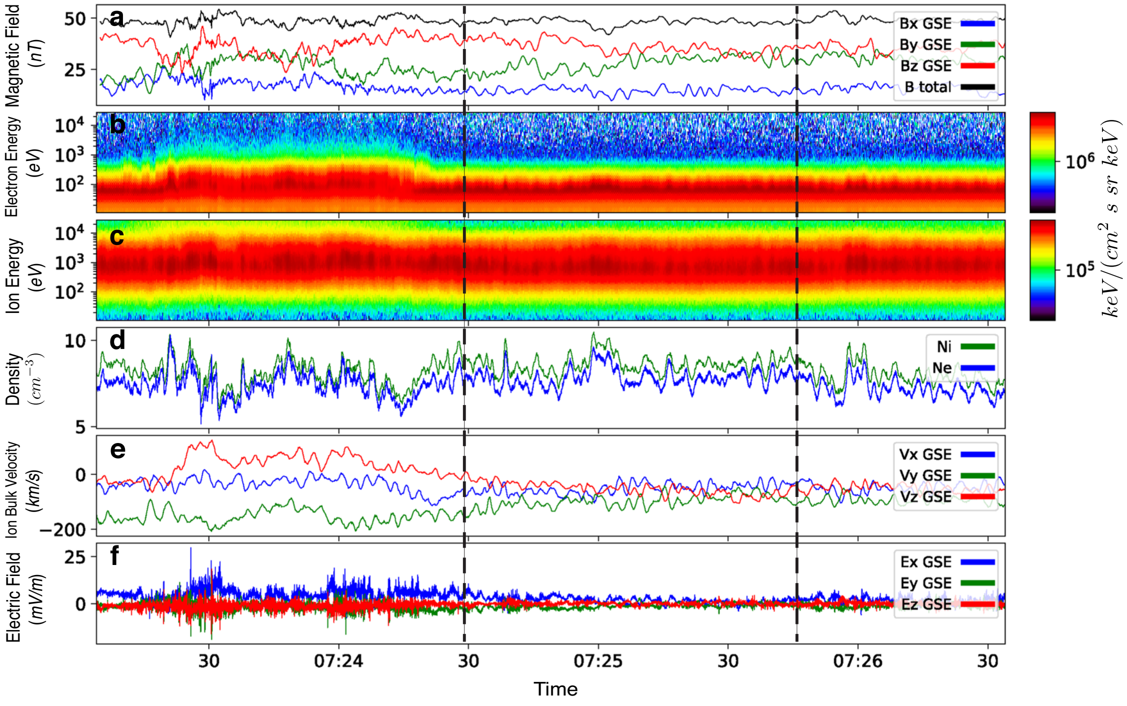

Fig. 1 | MMS observations of magnetosheath turbulence. Burst-mode data from MMS1 on 12 January 2016 starting at 07:23:04. **a** Magnetic field, (**b**) ion and (**c**) electron energy spectra, (**d**) ion and electron densities, (**e**) ion bulk velocity, and (**f**) electric field measurements. Dashed vertical lines delimit the 77 s interval analyzed here. Source data are provided as a Source Data file.

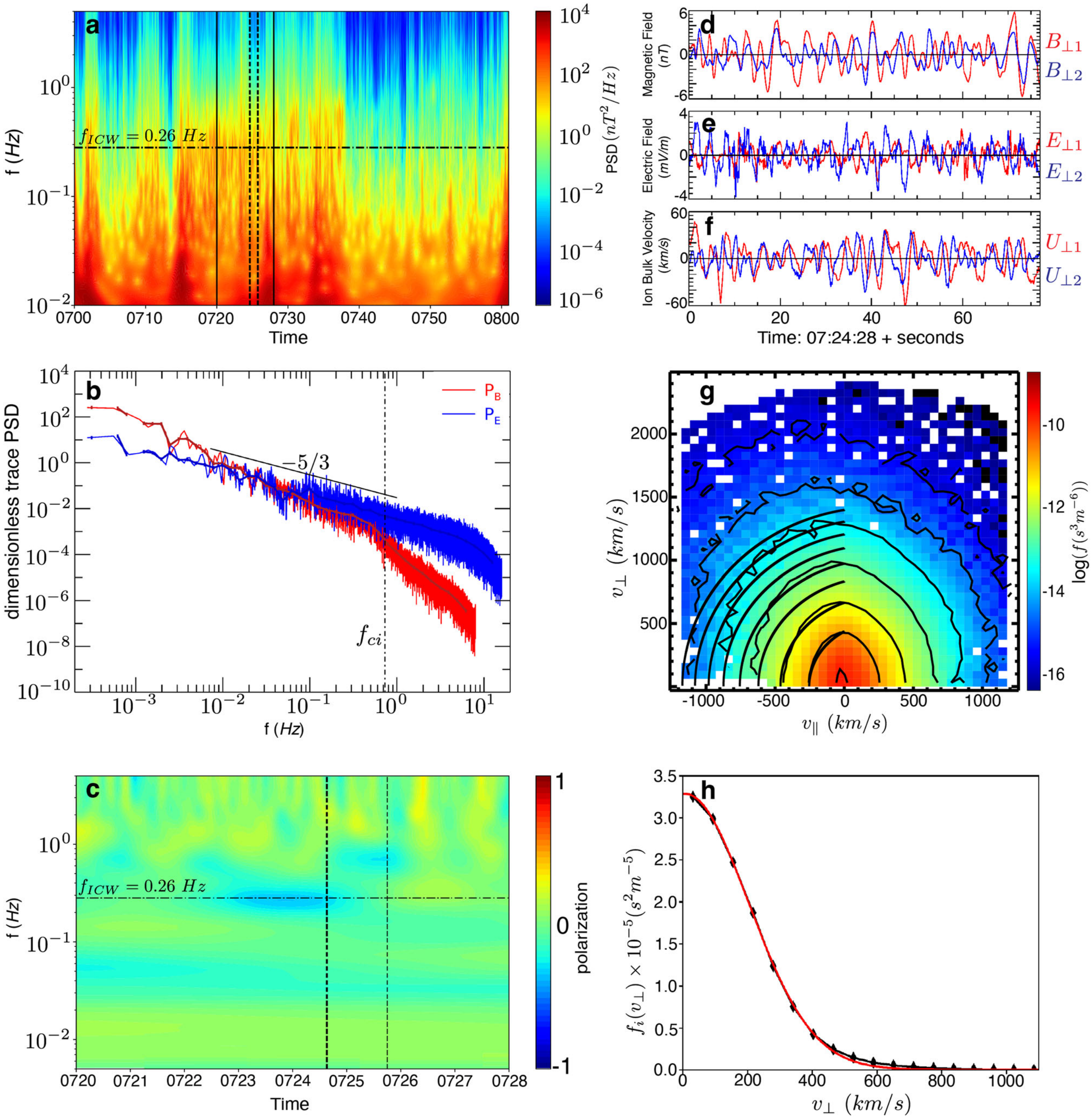

Fig. 2 | Evidence of ion cyclotron waves and ion distribution response. **a** Magnetic field energy spectrum from MMS1 over 07:00–08:00 on 12 January 2016. Solid vertical lines indicate the 8 minute interval shown in **c**, dashed vertical lines indicate the 77 s burst-mode interval analyzed in this work, horizontal dashed-dotted line indicates the ion cyclotron wave frequency. **b** Dimensionless trace PSD of magnetic field (P_B, red) and electric field (P_E, blue) with spectral index of −5/3 (black) shown, vertical dashed-dotted line indicates the ion cyclotron frequency. **c** Magnetic field polarization from 07:20–07:28, where dashed vertical lines indicate the 77 s burst-mode interval; significant left-hand polarization is observed at frequency $f_{ICW} \simeq 0.26$ Hz (horizontal dashed-dotted line). Perpendicular components of (**d**) the magnetic field, (**e**) electric field, and (**f**) ion bulk velocity, all high-pass filtered at $f_{cut} = 0.1$ Hz. **g** Background ion distribution $f_{0i}(v_\perp, v_\parallel)$ for the 77 s interval, with contours of constant energy (solid black) in the wave frame centered at $v_{ph} = 0.7 v_A$. **h** Reduced perpendicular ion distribution $f_{0i}(v_\perp)$ (black) with an overplotted Gaussian fit (red). Source data are provided as a Source Data file.

of approximately −5/3 at $f \lesssim 0.5$ Hz, in agreement with expectations for the turbulent inertial range at $k_\perp \rho_i < 1$ from modern theories for anisotropic plasma turbulence[45,46]. Analysis of the magnetic field polarization, calculated using the cross-coherence of the Morlet wavelet transform[43,44] and shown in Fig. 2c, shows a significant left-hand polarization at $f_{ICW} \simeq 0.26$ Hz (yielding an ICW period $T_{ICW} = 3.85$ s), consistent with the properties of ICWs. To highlight these left-hand polarized fluctuations, in Fig. 2d–f we plot the perpendicular components of the magnetic field $\mathbf{B}_\perp(t)$, electric field $\mathbf{E}_\perp(t)$, and ion bulk flow velocity $\mathbf{U}_{\perp i}(t)$ over the 77 s interval in a magnetic field-aligned coordinate (FAC) system in the reference frame of the mean ion bulk flow velocity (see Methods). We have also high-pass filtered the measurements at $f_{cut} = 0.1$ Hz to eliminate the larger amplitude, lower frequency fluctuations. The sense of left-handed polarization is most apparent in the $\pi/2$ phase shift between $U_{\perp 1}$ and $U_{\perp 2}$, Fig. 2e. Together this analysis supports a significant presence of ICWs in the turbulent fluctuations of this interval. The origin of these ICWs is unknown, and our direct measurements below show that they are damping in this

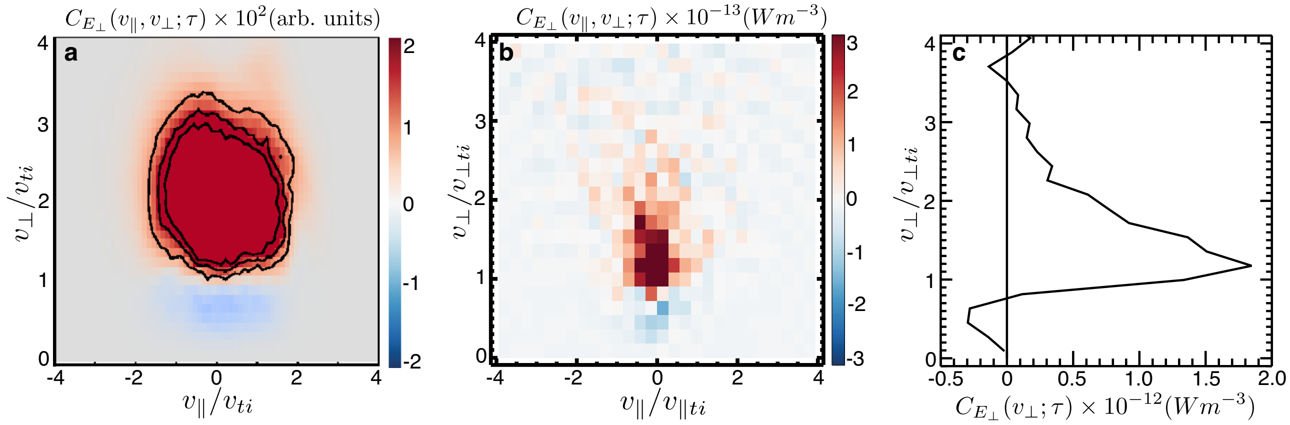

Fig. 3 | Gyrotropic velocity-space signature of ion cyclotron damping. The gyrotropic velocity-space signature of ion cyclotron damping $C_{E_\perp}(v_\parallel, v_\perp; \tau)$ from (**a**) a hybrid Vlasov–Maxwell (HVM) simulation of Alfvén-ion cyclotron turbulence[35] and from (**b**) the MMS data for a correlation interval $\tau = 77$ s. **c** Reduced correlation $C_{E_\perp}(v_\perp; \tau)$ for same interval of MMS data. Source data are provided as a Source Data file.

interval; we speculate that the ICWs were generated upstream via the Alfvén/ion cyclotron instablity[47] driven by the ion temperature anisotropy $T_{\perp i}/T_{\parallel i} > 1$ (see Supplementary Information (SI) Sec. S2), perhaps due to compression within a quasiperpendicular region of the bow shock, but analysis of the conditions upstream of the bow shock is inconclusive (see SI Sec. S4).

Furthermore, the time-averaged iVDF $f_{0i}(v_\parallel, v_\perp)$ is shown in Fig. 2g with circular contours of constant energy (solid black lines) plotted at $v_\parallel < 0$ in the frame of reference of an ICW with a parallel phase velocity of $v_{ph} = 0.7 v_A$, chosen to best fit the contours in the core of the iVDF. These contours serve as a qualitative guide along which the iVDF appears to be flattened, which is an indication of ICWs pitch-angle scattering the iVDF through cyclotron resonance[31,48]. In Fig. 2h, we show the reduced perpendicular iVDF $f_{0i}(v_\perp)$ (black), where we have integrated over the parallel velocity coordinate $v_\parallel$, with a Gaussian (red) plotted for comparison. A lack of flattening in the core at $v_\perp < v_{\perp ti}$ compared to the Gaussian argues against the possibility that stochastic ion heating is involved in damping the turbulent fluctuations[49,50].

Velocity-space signatures of ion cyclotron damping

To determine whether ion cyclotron damping plays a role in the damping of the turbulent fluctuations in this interval, we apply the FPC technique[32–35] to determine the velocity-space signature of the ion energization using the perpendicular field-particle correlation $C_{E_\perp}(\mathbf{v}, t; \tau)$ and to compute the rate of energy transfer to the ions. The FPC technique uses single-point measurements of the electric field and particle velocity distributions to determine the energy transfer to particles as a function of the particle velocity which can be used to identify the nature of the wave-particle interactions involved (see Methods for the detailed analysis procedure).

In our application of the FPC technique, we first determine the mean magnetic field $\mathbf{B}_0$ and mean ion bulk flow velocity $\mathbf{U}_{0i}$ over the full correlation interval $\tau = 77$ s, then Lorentz transform the fields $\mathbf{E}(t)$ and $\mathbf{B}(t)$ and iVDF $f_i(\mathbf{v}, t)$ to the mean ion bulk flow frame, and rotate these measurements into a magnetic FAC system. Next we compute the instantaneous alternative field-particle correlation $C'_{E_j}(\mathbf{v}, t; \tau = 0) = q_i v_j E_j(t) f_i(\mathbf{v}, t)$ where j indicates the vector component in the magnetic FAC system and the electric field E_j has been high-pass filtered at $f_{cut} = 0.1$ Hz (to eliminate oscillatory energy transfer[32–34]). These $C'_{E_j}(\mathbf{v}, t; \tau = 0)$ measurements are summed in Cartesian velocity bins, then the velocity-space derivatives are taken for each field component using (6) and combined to yield the perpendicular field-particle correlation $C_{E_\perp}(\mathbf{v}, t; \tau)$ in three-dimensional (3V) velocity space. Time-averages are computed by averaging the $C_{E_\perp}(\mathbf{v}, t; \tau)$ values in each velocity bin over the correlation interval τ.

The velocity-space signature of ion cyclotron damping in 2V gyrotropic space ($v_\parallel$, $v_\perp$) was found previously in numerical simulations[35,49,51], with an example reproduced in Fig. 3a. In Fig. 3b, we present the 2V gyrotropic correlation $C_{E_\perp}(v_\parallel, v_\perp; \tau)$ from this magnetosheath interval using a correlation interval equal to the full burst-mode interval, $\tau = 77$ s. This observed velocity-space signature shows a loss of phase-space energy density (blue) at $v_\perp/v_{\perp ti} \lesssim 1$ and a gain (red) over $1 \lesssim v_\perp/v_{\perp ti} \lesssim 3$. This pattern of energization in gyrotropic velocity-space in Fig. 3b agrees qualitatively with that found in Fig. 3a. Integrating over $v_\parallel$ yields the curve $C_{E_\perp}(v_\perp; \tau)$ in Fig. 3c, showing clearly that ions are gaining energy from the perpendicular electric field in the region where $C_{E_\perp}(v_\perp; \tau) > 0$ for $v_\perp/v_{\perp ti} \gtrsim 1$, consistent with ion cyclotron damping.

To assess whether the ion cyclotron damping is persistent in time over our correlation interval, in Fig. 4a we present a timestack plot of the instantaneous perpendicular correlation $C_{E_\perp}(v_\perp, t; \tau = 0)$, and in Fig. 4b the timestack plot of the time-averaged correlation $C_{E_\perp}(v_\perp, t; \tau = 16.5s)$ with $\tau \approx 4 T_{ICW}$ (corresponding to 110 iVDFs from the FPI DIS instrument). The instantaneous correlation $C_{E_\perp}(v_\perp, t; \tau = 0)$ includes a large oscillatory component of the energy transfer which obscures the net energization rate of ions. This oscillatory component is removed through time-averaging, and the persistent energization of ions is apparent in the time-averaged correlation $C_{E_\perp}(v_\perp, t; \tau = 16.5s)$, Fig. 4b, in velocity-space over $1 \lesssim v_\perp/v_{\perp ti} \lesssim 3$ lasting over the time range 30s $\lesssim t \lesssim$ 70 s. In Fig. 4c, the correlations are integrated over $v_\perp$, yielding the instantaneous $\int dv_\perp C_{E_\perp}(v_\perp, t; \tau = 0) = \mathbf{j}_{\perp,i} \cdot \mathbf{E}_\perp$ (black) and the time-averaged $\langle \mathbf{j}_{\perp,i} \cdot \mathbf{E}_\perp \rangle_\tau$ (red) rates of ion energization. While the net energization is difficult to assess in the instantaneous $\mathbf{j}_{\perp,i} \cdot \mathbf{E}_\perp$ (black), the time-averaged $\langle \mathbf{j}_{\perp,i} \cdot \mathbf{E}_\perp \rangle_\tau$ (red) unequivocally exposes net positive energization rates for the ions. Thus, the ion cyclotron damping is persistent in time and lasts more than 10 times as long as the ICW period. Furthermore, this energization appears to coincide in time with the disappearance of the ICW, as seen in Fig. 2c. Therefore, this FPC analysis presents the velocity-space signature of ion cyclotron damping as evidence of the damping of ICWs measured in the turbulent magnetosheath plasma, directly measuring the work done on the ions by the perpendicular electric field.

To demonstrate conclusively that ion cyclotron damping is playing a role in the dissipation of the fluctuations in magnetosheath turbulence, we integrate over $v_\parallel$ and plot the energization by both components of the perpendicular electric field in perpendicular velocity-space ($v_{\perp 1}$, $v_{\perp 2}$), shown in Fig. 5a $C_{E_{\perp 1}}(v_{\perp 1}, v_{\perp 2}; \tau)$ and Fig. 5b $C_{E_{\perp 2}}(v_{\perp 1}, v_{\perp 2}; \tau)$ correlated over the full interval $\tau = 77$ s (see Methods for definition of ($v_{\perp 1}$, $v_{\perp 2}$)). The quadrupolar velocity-space signatures presented in Fig. 5a, b are characteristic of ion cyclotron damping (as

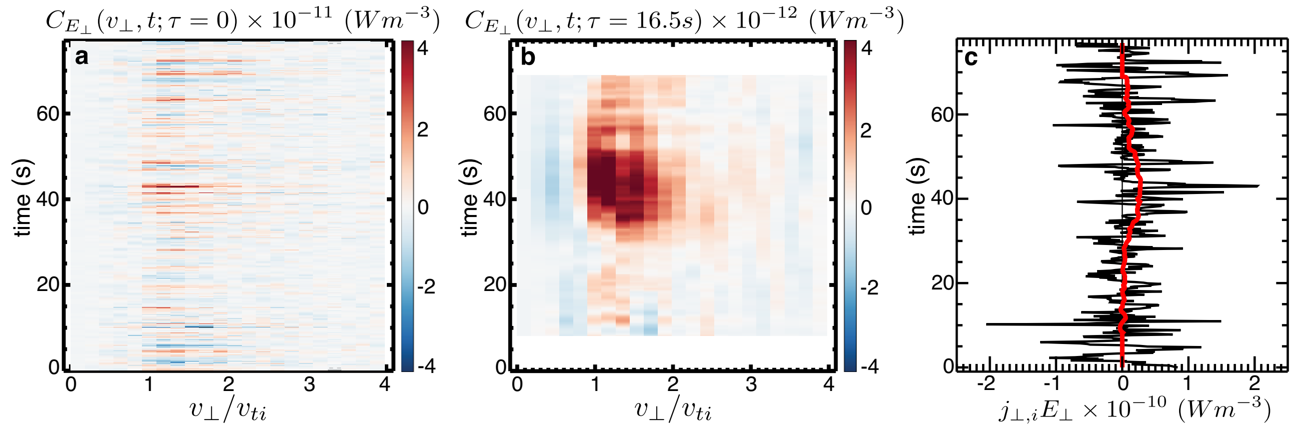

Fig. 4 | Timestack plot of ion cyclotron damping. Timestack plots of the perpendicular correlation $C_{E_\perp}(v_\perp,t;\tau)$ using both (**a**) instantaneous values (τ = 0) and (**b**) a correlation interval τ = 16.5 s. **c** The rate of ion energization by the perpendicular electric field $\langle \mathbf{j}_{\perp,i}\cdot\mathbf{E}_\perp\rangle_\tau$, computed both instantaneously with τ = 0 (black) and time-averaged over τ = 16.5 s (red). Source data are provided as a Source Data file.

discussed in detail for a fiducial case of ion cyclotron damping in the SI Sec. S1, with results for the plasma conditions of this magnetosheath interval shown in the next section), providing a new means to identify ion cyclotron damping using single-point spacecraft measurements.

Analytical model of ion cyclotron damping

To interpret the perpendicular velocity-space signatures $C_{E_{\perp1}}(v_{\perp1},v_{\perp2})$ and $C_{E_{\perp2}}(v_{\perp1},v_{\perp2})$ shown in Fig. 5a, b, we use solutions of the linear Vlasov–Maxwell dispersion relation for the Alfvén/ion cyclotron wave to generate a simple analytical prediction for comparison. First, we use the PLUME linear dispersion relation solver[52] to calculate the linear ICW frequency and damping rate for a fully ionized, hydrogenic plasma with bi-Maxwellian equilibrium velocity distributions with parameters based on the observed MMS interval: $\beta_{\parallel i}=0.383$, $T_{\parallel i}/T_{\parallel e}=6.84$, $T_{\perp i}/T_{\parallel i}=2.43$, $T_{\perp e}/T_{\parallel e}=0.973$, and $v_{\parallel ti}/c=7.34\times10^{-4}$. The ion temperature anisotropy leads to the unstable growth of wave modes with $0.3\lesssim k_\parallel\rho_{\perp i}\lesssim1.0$ and $k_\perp<k_\parallel$ through the proton cyclotron instability[47,52], where $\rho_{\perp i}=v_{\perp ti}/\Omega_i$ (see SI Fig. S5). Based on these estimates, we choose to model ICWs as a function of $k_\parallel d_i$ with $k_\perp d_i=0.016$ (note that the ion cyclotron damping rate is dominant and unchanged for all perpendicular wavenumbers $k_\perp d_i\lesssim0.5$), where the ion inertial length is defined by $d_i=v_A/\Omega_i=\rho_{\perp i}(T_{\parallel i}/T_{\perp i})^{1/2}\beta_{\parallel i}^{-1/2}$. Since our direct measurements in Fig. 4c unequivocally show damping of the measured ion cyclotron waves rather than unstable growth, we also calculate the eigenfunction for all of the same parameters but with an isotropic ion velocity distribution with $T_{\perp i}/T_{\parallel i}=1.0$. There are a couple of possible explanations why we observe wave damping rather than growth in the observed interval (see SI Sec. S2): (i) the clear presence of perpendicular wave motions can lead to an elevated perpendicular "apparent temperature"[53] in the measurements of the ion velocity distribution (see SI Fig. S6); and (ii) the fluctuation frequencies in the turbulence are faster than the predicted unstable wave growth rate, meaning that the instability is growing on a time-dependent background, so the linear dispersion relation predictions, which assume static background conditions, may not accurately predict the damping or growth rates of ICWs in this interval.

In Fig. 6a we plot the normalized wave frequency ω/Ω_i vs. $k_\parallel d_i$ for both cases $T_{\perp i}/T_{\parallel i}=1.0$ (dotted) and $T_{\perp i}/T_{\parallel i}=2.43$ (dashed) and Fig. 6b the normalized damping or growth rates $|\gamma|/\omega$. We find damping with $\gamma<0$ at all values of $k_\parallel d_i$ for the isotropic case (dotted), but unstable growth with $\gamma>0$ (red dashed) over $0.3\lesssim k_\parallel d_i\lesssim0.9$ for the anisotropic ion temperature case. For the isotropic case $T_{\perp i}/T_{\parallel i}=1.0$, in Fig. 6c, we decompose the total collisionless damping rate into the contributions from different collisionless damping mechanisms. We find that ion Landau damping (red short-dashed) and ion transit-time damping (red long-dashed) are very weak for this ICW mode, as well as all collisionless damping mechanisms with electrons (blue). Ion cyclotron damping (green dashed) dominates the damping for $k_\parallel d_i>0.3$, with significant damping rates of $-\gamma/\omega>0.1$ at parallel wavenumbers $k_\parallel d_i>0.6$. For the anisotropic ($k_\perp\gg k_\parallel$) fluctuations of the large-scale turbulent cascade, the ion damping at $k_\perp d_i\sim1$ via the Landau resonance for these parameters is expected to be very weak, with $-\gamma/\omega\lesssim4\times10^{-3}$ (see SI Sec. S6 and Fig. S9).

Using the measured magnetic field direction and ion bulk flow velocity, we estimate the parallel wavenumber of the ICW to fall within the range $0.5\lesssim k_\parallel d_i\lesssim1.5$ (see SI Sec. S3), which is consistent with the linear dispersion relation solutions in Fig. 6c showing significant ion cyclotron damping rates at $k_\parallel d_i\gtrsim0.6$. Note that an increasing value of $k_\parallel d_i$ yields a stronger damping rate due the perpendicular ion bulk flow and electric field fluctuations becoming increasingly more in phase, which leads to a skew in the quadrupolar signatures in the perpendicular plane ($v_{\perp1}$, $v_{\perp2}$) (see SI Sec. S1 and Fig. S2 for examples). For the measured plasma parameters, but with $T_{\perp i}/T_{\parallel i}=1.0$ to yield damping as observed, we choose a value $k_\parallel d_i=0.8$ with $k_\perp d_i=0.016$ (to satisfy the condition $k_\parallel/k_\perp\gg1$ for waves driven unstable by ion temperature anisotropy, see SI Sec. S2 and Fig. S5) which appears to produce the best agreement with the observations. Choosing a value of $E_{\perp1}/B_0v_A=0.15$ to match the observational amplitude of the ICW, the PLUME eigenfunction calculation yields values for the analytical model (see Methods) of $E_{\perp2}/B_0v_A=0.15$, $\phi=-\pi/2$, $U_{\perp1}/v_A=U_{\perp2}/v_A=0.62$, and $\delta_1=\delta_2=-0.44\pi$. Using these parameters and averaging the velocity-space signatures over one ICW period yields the perpendicular velocity-space signatures in Fig. 5c $C_{E_{\perp1}}(v_{\perp1},v_{\perp2})$ and Fig. 5d $C_{E_{\perp2}}(v_{\perp1},v_{\perp2})$.

These analytically predicted quadrupolar perpendicular velocity-space signatures in Fig. 5c and d show excellent qualitative agreement with the observed signatures presented in Fig. 5a and b, including the sight skew of the red regions across $v_{\perp2}=0$ in $C_{E_{\perp1}}(v_{\perp1},v_{\perp2})$ and across $v_{\perp1}=0$ in $C_{E_{\perp2}}(v_{\perp1},v_{\perp2})$. Note that the quadrupolar appearance is a consequence of the phase relations between the perpendicular electric field and ion bulk velocity components (as illustrated in SI Fig. S3). Furthermore, the sum of these quadrupolar signatures, $C_{E_{\perp1}}(v_{\perp1},v_{\perp2})+C_{E_{\perp2}}(v_{\perp1},v_{\perp2})$, yields energization of ions from $v_\perp<v_{\perp ti}$ to $v_\perp>v_{\perp ti}$, consistent with the intuitive expectation of perpendicular energization of the ions by ion cyclotron damping (see SI Fig. S4). It is important to note that, once the plasma parameters and wavevector of the ICW have been specified, the only free parameter left in determining these velocity space signatures is the overall wave amplitude, characterized by the parameter $E_{\perp1}/B_0v_A$; the quadrupolar appearance is a consequence of the self-consistently determined phase and amplitude relationships among the perpendicular electric field and ion

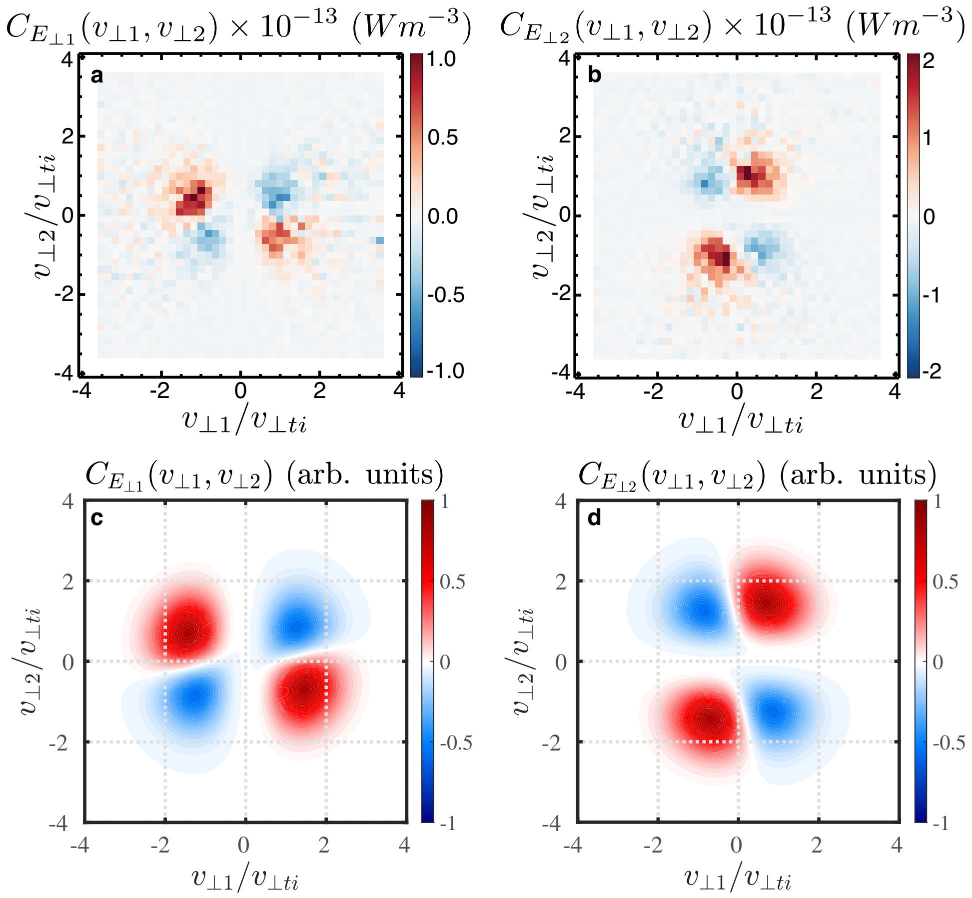

Fig. 5 | Perpendicular velocity-space signatures of ion cyclotron damping. From the MMS measurements, the perpendicular velocity-space signatures (**a**) $C_{E_{\perp 1}}(v_{\perp 1}, v_{\perp 2}; \tau)$ and (**b**) $C_{E_{\perp 2}}(v_{\perp 1}, v_{\perp 2}; \tau)$ over correlation interval $\tau = 77$ s. Analytical model prediction using the eigenfunction solutions of the Vlasov–Maxwell dispersion relation of the perpendicular velocity-space signatures of ion cyclotron damping, (**c**) $C_{E_{\perp 1}}(v_{\perp 1}, v_{\perp 2})$ and (**d**) $C_{E_{\perp 2}}(v_{\perp 1}, v_{\perp 2})$ averaged over one wave period, showing a qualitatively similar pattern as the MMS measurements. Source data are provided as a Source Data file.

bulk velocity components. Thus, this analytical prediction demonstrates that these two quadrupolar signatures in the $(v_{\perp 1}, v_{\perp 2})$ plane represent the perpendicular velocity-space signature of ion cyclotron damping. Along with the signature in gyrotropic velocity-space $(v_\parallel, v_\perp)$ shown in Fig. 3b, these velocity-space signatures enable us to identify definitively ion cyclotron damping of the turbulent fluctuations in space plasmas using single-point spacecraft measurements.

Discussion

We can use these results to distinguish and identify mechanisms of turbulent dissipation. Direct in situ measurements of the electric field and ion current density in a turbulent space plasma can be used to determine the net rate of work done on the ions by the electric field; in Fig. 4c, we have shown significant perpendicular energization of the ions, $\mathbf{j}_{\perp,i} \cdot \mathbf{E}_\perp > 0$. But both ion cyclotron damping[15] and stochastic ion heating[17,49,51,54] are potential mechanisms that can damp the turbulent fluctuations at the scale of the ion Larmor radius and energize ions via the perpendicular component of the electric field. The FPC technique provides a practical means for distinguishing different physical mechanisms of particle energization through the features of their velocity-space signatures, such as electron Landau damping[13,37,55] or ion cyclotron damping[35].

Several lines of evidence enable us to rule out a significant contribution by stochastic ion heating in this magnetosheath interval. First, theoretical considerations suggest that stochastic ion heating largely energizes ions in the core of the velocity distribution at $v_\perp/v_{\perp ti} < 1$[17,50], flattening the core of the iVDF relative to a Maxwellian; evidence from hybrid numerical simulations supports this hypothesis[49,51]. The reduced perpendicular iVDF in Fig. 2h shows no evidence for this predicted impact of stochastic ion heating. Second, the gyrotropic velocity-space signature $C_{E_\perp}(v_\parallel, v_\perp; \tau)$ in Fig. 3b instead shows ion energization over the range $1 \lesssim v_\perp/v_{\perp ti} \lesssim 3$, inconsistent with the expectation for stochastic ion heating but consistent with the expectation for ion cyclotron damping from numerical simulations, as shown in Fig. 3a[35]. Finally, the predictions for the stochastic ion heating rate (see next section) are also much smaller than the ion energization rate measured in the interval presented here.

A key result of this study is the observational determination of the velocity-space signature of ion cyclotron damping with these distinguishing features: (i) in the gyrotropic velocity-space signature $C_{E_\perp}(v_\parallel, v_\perp; \tau)$ in Fig. 3b, a pattern showing the loss of phase-space energy density at $v_\perp/v_{ti} \lesssim 1$ (blue) and gain at $1 \lesssim v_\perp/v_{ti} \lesssim 3$ (red); and (ii) in the perpendicular velocity-space signatures $C_{E_{\perp 1}}(v_{\perp 1}, v_{\perp 2}; \tau)$ and $C_{E_{\perp 2}}(v_{\perp 1}, v_{\perp 2}; \tau)$ in Fig. 5a,b, the appearance of quadrupolar signatures showing ion energization in opposite quadrants for $E_{\perp 1}$ and $E_{\perp 2}$, in agreement with analytical predictions for ion cyclotron damping of ICWs using a Vlasov–Maxwell linear dispersion relation solver, as shown in Fig. 5c,d. These velocity-space signatures uniquely identify that ion cyclotron damping is acting to dissipate the fluctuations in the turbulent magnetosheath plasma during this MMS observation, establishing a critical foundation for distinguishing different physical mechanisms of ion energization. The timestack plot $C_{E_\perp}(v_\perp, t; \tau)$ in Fig. 4b, averaged over a correlation interval $\tau \approx 4T_{ICW}$, shows clearly that there is persistent perpendicular energization of the ions over an

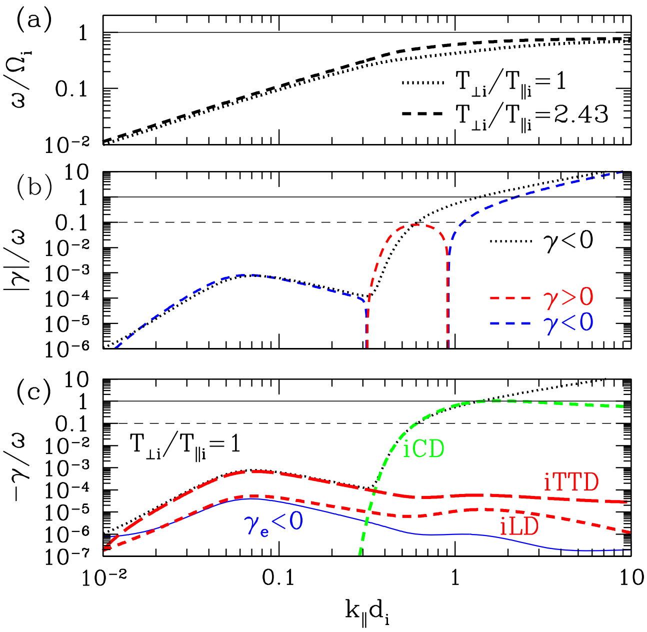

Fig. 6 | Vlasov–Maxwell frequencies and damping/growth rates. a Normalized wave frequency ω/Ω_i for $T_\perp/T_{\parallel i} = 1.0$ (dotted) and $T_\perp/T_{\parallel i} = 2.43$ (dashed) vs. normalized parallel wavenumber $k_\parallel d_i$ with fixed $k_\perp d_i = 0.016$. **b** For $T_\perp/T_{\parallel i} = 1.0$, damping $\gamma < 0$ (black dotted) occurs for all $k_\parallel d_i$, but for $T_\perp/T_{\parallel i} = 2.43$, unstable growth with $\gamma > 0$ (red dashed) occurs over $0.3 \lesssim k_\parallel d_i \lesssim 0.9$, with damping $\gamma < 0$ (blue dashed) outside that range. **c** For $T_\perp/T_{\parallel i} = 1.0$, decomposition of the total damping rate (black dotted): total electron damping γ_e (blue), ion Landau damping (iLD, red short-dashed), ion transit-time damping (iTTD, red long-dashed), and ion cyclotron damping (iCD, green dashed). Source data are provided as a Source Data file.

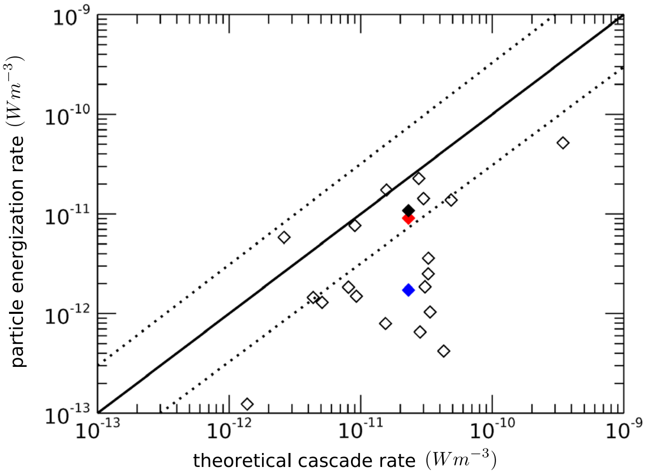

Fig. 7 | The particle energization rate versus the theoretical cascade rate ϵ. The solid line represents particle energization rates equal to the estimated turbulent cascade rate ϵ, with the dotted lines indicating the range of the order-of-magnitude estimate of ϵ. We plot the parallel electron energization rates $\langle j_{\parallel,e}E_\parallel\rangle_\tau$ from twenty intervals in Afshari et al. (open diamonds), highlighting $\langle j_{\parallel,e}E_\parallel\rangle_\tau$ from the interval analyzed here (their Interval 02, blue diamond)[37]. The perpendicular ion energization $\langle \mathbf{j}_{\perp,i} \cdot \mathbf{E}_\perp\rangle_\tau$ (red diamond) by ion cyclotron damping is plotted along with the sum of ion and electron energization rates (black diamond). Source data are provided as a Source Data file.

extended duration, lasting approximately ten times the measured ICW period of $T_{ICW} = 3.85$ s. Together, these lines of evidence constitute the first measurement of ion cyclotron damping in a turbulent space plasma through a direct determination of the work done by the perpendicular electric field on the ions.

With the ability to identify different mechanisms of particle energization, we are able to quantify the different channels of turbulent energy dissipation. In order to develop predictive models of plasma turbulent heating and the resulting partitioning of energy among the plasma species, a critical first step is to identify the different mechanisms of energization responsible for damping the turbulence as a function of the plasma and turbulence parameters. Applying the FPC technique to spacecraft observations provides a viable means to achieve the identification of all physical mechanisms that contribute to damping the turbulence and to compute the resulting particle energization rates by species. Here we propose a working definition of the turbulence as all of the physical mechanisms that serve to mediate the conversion of the energy of large-scale plasma flows and electromagnetic fields into heat of the plasma species, including both the local energy transfer by the turbulent cascade and any nonlocal energy transfer via kinetic instabilities. We adopt this definition because, in a practical sense, it is not generally possible to separate observationally whether the measured turbulent fluctuations were driven by local or nonlocal energy transfer. Our estimate of the cascade rate ϵ is based on the measured turbulent amplitudes that includes fluctuations from both sources, so the observed dissipation rate may be compared to this turbulent cascade rate.

In Afshari et al., twenty MMS burst-mode intervals of magnetosheath turbulence were analyzed, finding the velocity-space signature of electron Landau damping in nineteen of the twenty intervals[37]. The electron energization rates due to the parallel component of the electric field were plotted against the estimated turbulent energy cascade rate ϵ (computed using (7), see Methods), as shown in Fig. 7, where the open diamonds correspond to each of these measurements. The blue diamond denotes the electron energization rate due to Landau damping $\langle j_{\parallel,e}E_\parallel\rangle_\tau = 1.7 \times 10^{-12}$ W m^{-3} for Interval 02 in that study, the same interval analyzed here, and the estimated cascade rate for this interval[37] is $\epsilon = 23 \times 10^{-12}$ W m^{-3}. Since the calculation of the turbulent cascade rate—based on a cascade model of critically balanced, anisotropic plasma turbulence[56,57]—is simply an order-of-magnitude estimate, any points falling within the diagonal dotted lines (factors of three above or below the predicted ϵ) represent significant dissipation rates of the same order as the turbulent cascade rate. The interval-averaged rate of ion energization by the dissipation of the turbulent fluctuations via ion cyclotron damping computed here yields $\langle \mathbf{j}_{\perp,i} \cdot \mathbf{E}_\perp\rangle_\tau = 9.1 \times 10^{-12}$ W m^{-3} (red diamond), and the sum of the electron Landau damping and ion cyclotron damping yields 10.8×10^{-12} W m^{-3} (black diamond), agreeing to order of magnitude with the estimated turbulent cascade rate ϵ.

For context, let us determine the potential contributions from other proposed mechanisms of turbulent dissipation. Using a procedure analogous to Chen et al.[13] to analyze the parallel energization of the ions via Landau damping, we obtain a rate $\langle j_{\parallel,i}E_\parallel\rangle_\tau \sim 10^{-14}$ W m^{-3}, which is below the estimated noise floor for these measurements (see Fig. 8 in the Methods section). This result indicates negligible ion Landau damping, consistent with the linear collisionless damping rate prediction with $-\gamma/\omega \lesssim 4 \times 10^{-3}$ for the anisotropic turbulent fluctuations with $k_\perp \gg k_\parallel$ from the large-scale cascade in this interval (see SI Sec. S6 and Fig. S9). In principle, we could use the FPC technique to estimate the electron cyclotron damping of turbulent fluctuations via $E_\perp$ using $C_{E_\perp,e}$, but we do not attempt this determination for two reasons: (i) the Nyquist frequency of the sampling interval for the electron velocity distribution, $f_{Ny} \simeq 16$ Hz, is much less than the electron cyclotron frequency, $f_{ce} = 1.34$ kHz, so the measurement cadence is much too small to obtain reliable results[58]; and (ii) the observed energy in turbulent fluctuations with $f \sim f_{ce}$ is about two orders of magnitude lower than the energy at $f < 100$ Hz, so theoretical arguments suggest that turbulent dissipation by electron cyclotron damping is negligible. We can estimate the rate of

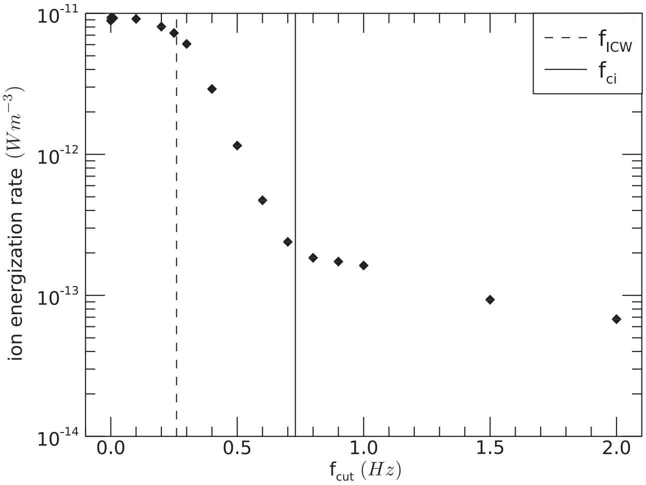

Fig. 8 | Ion energization rate as a function of cut-off frequency. Time-averaged rate of work done on the ions by the perpendicular electric field $\langle \mathbf{j}_{\perp,i}\cdot\mathbf{E}_\perp\rangle_\tau$ vs. the high-pass cut off frequency f_{cut}. Source data are provided as a Source Data file.

stochastic ion heating using

$$Q_{\perp,stoch} = n_i m_i \frac{c_1(\delta v_i)^3}{\rho_i} e^{-c_2/\epsilon_i} \tag{1}$$

from Bourouaine and Chandran[59], where $c_1 = 0.75$, $c_2 = 0.34$, $\delta v_i = 30$ km/s is the amplitude of the ion velocity fluctuations at the scale of the ion Larmor radius $\rho_i = 75$ km from Fig. 2f, and $\epsilon_i = \delta v_i/v_{\perp ti} = 0.087$. The resulting value $Q_{\perp,stoch} = 8.0\times10^{-14}$W m^{-3} is negligible compared to the measured ion energization rates, providing a strong argument that stochastic ion heating plays no role. It has been recently shown that, in $\beta \gg 1$ plasmas, kinetic temperature instabilities can generate an enhanced effective collisionality that leads to anisotropic "viscous" heating of large-scale turbulent fluctuations[20], but that mechanism does not apply to our comparison to the turbulent cascade rate for two reasons: (i) our parallel ion plasma beta $\beta_{\parallel i} = 0.383$ is too low for this mechanism to be effective; and (ii) we estimate the turbulent cascade rate at $f = 0.2$ Hz[37] at the end of the inertial range, so any energy removed by large-scale viscous heating would not appear in our estimate turbulent cascade rate.

In summary, application of the FPC technique to this MMS interval produces unique velocity-space signatures, enabling us to identify ion cyclotron damping and electron Landau damping as the dominant physical mechanisms removing energy from the turbulence. In addition to providing the first direct measurement of ion cyclotron damping of turbulence in a space plasma, we have shown that the resulting ion and electron energization rates from these mechanisms sum to yield order-of-magnitude agreement with the predicted turbulent cascade rate. Thus, we have identified the key channels of turbulent dissipation and particle energization, as well as directly measured the partitioning of dissipated turbulent energy between the ions and electrons. Application of the FPC analysis to a larger statistical sample of spacecraft measurements provides a viable means to identify the dominant dissipation mechanisms and to characterize the partitioning of energy among species as a function of the plasma and turbulence parameters, a critical step in the development of a predictive theory of turbulent dissipation and plasma heating in space and astrophysical plasmas.

Methods

Field-particle correlation technique

The field-particle correlation (FPC) technique combines the electromagnetic fields and particle velocity distributions measured at a single point in space to determine a velocity-space signature the can be used to identify the mechanism of particle energization and to determine the rate of collisionless energy transfer between the fields and particles[32–35]. The technique has been applied to explore the collisionless damping of plasma waves[1,32,33], the damping of kinetic plasma turbulence in numerical simulations[34,35,55,60] and spacecraft observations[13,37], the acceleration of particles in numerical simulations of collisionless shocks[61,62], the acceleration of auroral electrons by Alfvén waves in laboratory experiments[63], and electron heating in collisionless magnetic reconnection[64].

Multiplying the Vlasov equation by $m_s v^2/2$, we obtain an equation

$$\frac{\partial w_s}{\partial t} = -\mathbf{v}\cdot\nabla w_s - q_s\frac{v^2}{2}\mathbf{E}\cdot\frac{\partial f_s}{\partial \mathbf{v}} - q_s\frac{v^2}{2}\mathbf{v}\times\mathbf{B}\cdot\frac{\partial f_s}{\partial \mathbf{v}} \tag{2}$$

that dictates the rate of change of the 3D-3V phase-space energy density of species s, $w_s(\mathbf{r}, \mathbf{v}, t) \equiv m_s v^2 f_s(\mathbf{r}, \mathbf{v}, t)/2$, where $f_s(\mathbf{r}, \mathbf{v}, t)$ is velocity distribution function for species s, q_s and m_s are the charge and mass, $\mathbf{r}$ is the spatial position, $\mathbf{v}$ is the velocity coordinate, and $\mathbf{E}(\mathbf{r}, t)$ and $\mathbf{B}(\mathbf{r}, t)$ are the electric and magnetic fields, respectively. Only the electric field term (middle term on the right-hand side of (2)) leads to a net change in the energy of species s[32–34].

Therefore, in a magnetic field aligned coordinate (FAC) system (see below) with unit vectors $(\hat{\mathbf{e}}_\parallel, \hat{\mathbf{e}}_{\perp1}, \hat{\mathbf{e}}_{\perp2})$, we define the FPC with each component j = 1, 2 of the perpendicular electric field $C_{E_{\perp j},s}$ over a correlation interval τ at a single position $\mathbf{r}_0$ by

$$C_{E_{\perp j},s}(\mathbf{r}_0,\mathbf{v},t;\tau) = \frac{1}{\tau}\int_{t-\tau/2}^{t+\tau/2} dt' \frac{-q_s}{2} v_{\perp j}^2 \frac{\partial f_s(\mathbf{r}_0,\mathbf{v},t')}{\partial v_{\perp j}} E_{\perp j}(\mathbf{r}_0,t'), \tag{3}$$

where the total energization by the perpendicular components of the electric field is given by $C_{E_\perp,s}(\mathbf{r}_0,\mathbf{v},t;\tau) = C_{E_{\perp1},s}(\mathbf{r}_0,\mathbf{v},t;\tau) + C_{E_{\perp2},s}(\mathbf{r}_0,\mathbf{v},t;\tau)$.

The integration of $C_{E_\perp,s}(\mathbf{r}_0,\mathbf{v},t;\tau)$ over 3V velocity space yields

$$\int d^3\mathbf{v}\, C_{E_\perp,s}(\mathbf{r}_0,\mathbf{v},t;\tau) = \langle \mathbf{j}_{\perp,s}(\mathbf{r}_0,t)\cdot\mathbf{E}_\perp(\mathbf{r}_0,t)\rangle_\tau, \tag{4}$$

the rate of work done on species s by the perpendicular electric field at position $\mathbf{r}_0$ averaged over the correlation interval τ. Note that the replacement of v^2 in the electric field term of (2) by $v_{\perp j}^2$ in (3) does not change the net velocity-integrated rate of energy transfer, but does help to highlight the regions in velocity space that govern the net energization of the particles[61].

At position $\mathbf{r}_0$, $C_{E_\perp,s}(\mathbf{r}_0,\mathbf{v},t;\tau)$ is a four-dimensional function in 3V velocity space $\mathbf{v}$ and time t, so reduction to fewer dimensions is beneficial for visualization and analysis. Converting to a cylindrical FAC system with $v_\perp = \sqrt{v_{\perp1}^2 + v_{\perp2}^2}$, and integrating over the gyrophase angle about the mean magnetic field $\mathbf{B}_0$, we obtain a gyrotropic velocity-space signature, $C_{E_\perp,s}(v_\parallel,v_\perp;\tau)$, where we have suppressed spatial position dependence and taken the correlation interval to be the full burst-mode interval $\tau = 77$ s. We can further integrate over $v_\parallel$ to obtain $C_{E_\perp,s}(v_\perp;\tau)$. Alternatively, we can instead correlate over sub-intervals $\tau \ll 77$ s, and integrate over gyrophase angle and $v_\parallel$ to obtain a time-stack plot, $C_{E_\perp,s}(v_\perp,t;\tau)$, to assess the particle energization by $E_\perp$ as a function of $v_\perp$ over time. Finally, we can return to the Cartesian FAC system $(\hat{\mathbf{e}}_\parallel, \hat{\mathbf{e}}_{\perp1}, \hat{\mathbf{e}}_{\perp2})$, correlate over the full interval $\tau = 77$ s, and integrate over $v_\parallel$ to obtain the perpendicular velocity-space signature, $C_{E_\perp,s}(v_{\perp1},v_{\perp2};\tau)$, which is essential in positively identifying ion cyclotron damping in the analysis here.

FPC implementation using spacecraft measurements

For the 77 s burst-mode interval, we time-average the instantaneous magnetic field measurements in GSE coordinates by the FGM instrument[39] to determine a mean magnetic field direction $\mathbf{B}_0 = \langle \mathbf{B}(t)\rangle_\tau$, where angle brackets $\langle \ldots \rangle_\tau$ denote an average over the full time interval τ = 77 s. Similarly, we compute the mean ion bulk flow velocity by $\mathbf{U}_{0i} = \langle \mathbf{U}_i(t)\rangle_\tau$. We then define a local FAC system by $(\hat{\mathbf{e}}_\parallel, \hat{\mathbf{e}}_{\perp 1}, \hat{\mathbf{e}}_{\perp 2})$, where $\hat{\mathbf{e}}_\parallel = \mathbf{B}_0/|\mathbf{B}_0|$, and $\hat{\mathbf{e}}_{\perp 1} = (\mathbf{B}_0 \times \mathbf{U}_{0i}) \times \mathbf{B}_0 / |(\mathbf{B}_0 \times \mathbf{U}_{0i}) \times \mathbf{B}_0|$, and $\hat{\mathbf{e}}_{\perp 2} = \mathbf{B}_0 \times \mathbf{U}_{0i} / |\mathbf{B}_0 \times \mathbf{U}_{0i}|$.

The electric field is measured at 8192 Hz in GSE coordinates by the EDP instrument suite[40,41,65]. The electric field measurements in the spacecraft frame (primed), $\mathbf{E}'(\mathrm{t})$, are Lorentz transformed[66,67] to the mean ion bulk flow frame (unprimed), $\mathbf{E}(\mathrm{t}) = \mathbf{E}'(t) + \mathbf{U}_{0i} \times \mathbf{B}(\mathrm{t})$. The $\mathbf{E}(\mathrm{t})$ is down-sampled (by averaging) to 150 ms to match the cadence of FPI Dual Ion Spectrometer (DIS)[42], and rotated into the FAC system to obtain $E_{\perp 1}(t)$ and $E_{\perp 2}(t)$. The iVDF measurements $f_i(\mathbf{v}, t)$ are likewise transformed to the mean ion bulk flow frame and rotated into the FAC system. To remove the large-amplitude signal of oscillatory energy transfer by large-scale, low-frequency electric fields[32–34], we high-pass filter our time series $\mathbf{E}(t)$ at f_{cut} = 0.1 Hz using a 5th-order Butterworth filter.

Next, for each DIS measurement interval, we compute the alternative field-particle correlation[33,68] with τ = 0 for each electric field component $E_j(t)$ in the FAC system, given by

$$C'_{E_j}(\mathbf{v}, t; \tau = 0) = q_i v_j E_j(t) f_i(\mathbf{v}, t), \tag{5}$$

where q_i is the ion charge (assumed to be protons), and v_j is each velocity coordinate in the FAC system. To convert from the alternative FPC $C'_{E_j}(\mathbf{v}, t; \tau = 0)$ to the standard FPC $C_{E_j}(\mathbf{v}, t; \tau)$, we first create a Cartesian grid of bins in FAC velocity-space $(v_\parallel, v_{\perp 1}, v_{\perp 2})$ with bin width $\Delta v / v_{ti}$ = 0.2. At each DIS measurement time t, the instantaneous $C'_{E_j}(\mathbf{v}, t; \tau = 0)$ values falling within each velocity bin are summed. We use finite differencing between velocity bins to compute the derivatives[13] for each component E_j,

$$C_{E_j}(\mathbf{v}, t; \tau) = -\frac{v_j}{2} \frac{\partial C'_{E_j}(\mathbf{v}, t; \tau)}{\partial v_j} + \frac{C'_{E_j}(\mathbf{v}, t; \tau)}{2}. \tag{6}$$

To obtain the final perpendicular FPC given by (3), we sum the two perpendicular components $C_{E_\perp}(\mathbf{v}, t; \tau) = C_{E_{\perp 1}}(\mathbf{v}, t; \tau) + C_{E_{\perp 2}}(\mathbf{v}, t; \tau)$. Subsequently, to obtain a time-averaged $C_{E_j}(\mathbf{v}; \tau)$, the values of $C_{E_j}(\mathbf{v}; \tau)$ in each velocity bin are time-averaged over any chosen interval of length τ.

As a consistency check that the rate of ion energization by $E_\perp$ computed here is indeed due to ion cyclotron damping, we adjust the cut-off frequency f_{cut} of the high-pass filtered electric field and compute the resulting averaged rate of ion energization $\langle \mathbf{j}_{\perp,i} \cdot \mathbf{E}_\perp \rangle_\tau$ for τ = 77 s, shown in Fig. 8. These results clearly show that nearly all the energy is lost over the frequency range $f_{ICW} \le f \le f_{ci}$, as expected for ion cyclotron damping. Furthermore, when the electric field is high-pass filtered at $f_{cut} > f_{ci}$ in Fig. 8, the ion energization rate levels out at approximately 10^{-13} W m^{-3}, which we take to be the noise floor of energization rate calculations using the FPC technique.

Turbulent energy cascade model

Using a cascade model for turbulence[56,57], we estimate the turbulent energy cascade rate ϵ in the inertial range given by[37]

$$\epsilon \sim \frac{\text{Energy Density}}{\text{Cascade Time}} = \frac{n_0 m_p U_\perp^2}{1/(k_\perp U_\perp)} = n_0 m_p \left(\frac{2\pi f}{v_{\perp,sc}}\right) \frac{[\delta \hat{B}_\perp(f)]^3}{(\mu_0 n_0 m_p)^{3/2}} \tag{7}$$

where n_0 is the ion number density, m_p is the proton mass, f = 0.2 Hz is the frequency within the inertial range, $\delta \hat{B}_\perp(f)$ is the amplitude of the magnetic field fluctuations computed at a frequency f using an increment with lag t = 5 s. The turbulent energy density includes both kinetic and magnetic contributions, which are assumed equal for Alfvénic turbulence, and the cascade time is calculated within the turbulent inertial range at $f \simeq 0.2$ Hz.

Analytical model

Here we develop an analytical model that uses the phase and amplitude eigenfunction relations between the perpendicular electric field components $E_{\perp 1}$ and $E_{\perp 2}$ and the perpendicular ion bulk velocity components $U_{\perp 1,i}$ and $U_{\perp 2,i}$ to generate a prediction of the velocity-space signature in the $(v_{\perp 1}, v_{\perp 2})$ plane. First, we define a local magnetic FAC system $(\hat{\mathbf{e}}_\parallel, \hat{\mathbf{e}}_{\perp 1}, \hat{\mathbf{e}}_{\perp 2})$. The components of the electric field and ion fluid velocity in the $(\hat{\mathbf{e}}_{\perp 1}, \hat{\mathbf{e}}_{\perp 2})$ plane can be specified by

$$E_{\perp 1} = E_1 \cos(\omega t); \qquad E_{\perp 2} = E_2 \cos(\omega t - \phi), \tag{8}$$

$$U_{\perp 1,i} = U_1 \cos(\omega t - \delta_1); \qquad U_{\perp 2,i} = U_2 \cos(\omega t - \phi - \delta_2). \tag{9}$$

Given the amplitude E_1, the eigenfunction from the Vlasov–Maxwell linear dispersion relation specifies: (i) the wave frequency ω, (ii) the amplitudes of the other components E_2, U_1, and U_2, (iii) ϕ the phase shift between $E_{\perp 1}$ and $E_{\perp 2}$, and (iv) the δ_j is the phase shift between $E_{\perp j}$ and $U_{\perp j}$. The rate of ion energization by the perpendicular components of the electric field is given by $\mathbf{j}_{\perp,i} \cdot \mathbf{E}_\perp = q_i U_{\perp 1,i} E_{\perp 1} + q_i U_{\perp 2,i} E_{\perp 2}$, where the right-hand side shows the separate contributions from the two components. To generate predicted velocity-space signatures using the FPC technique, the iVDF is taken to be a shifted Maxwellian with a characteristic perpendicular thermal velocity $v_{\perp ti}$ and a perpendicular ion bulk velocity given by the self-consistent PLUME[52] eigenfunction for $\mathbf{U}_{\perp,i}$.

For this model, a left-hand circularly polarized wave has $E_1 = E_2$ and $\phi = -\pi/2$. In the low-frequency limit $\omega \ll \Omega_i$, the ion fluid velocity is given by the $\mathbf{E} \times \mathbf{B}$ velocity, such that $U_{\perp 1,i} = E_{\perp 2}/B$ and $U_{\perp 2,i} = -E_{\perp 1}/B$, which yields $\delta_1 = \delta_2 = -\pi/2$. In this case, the rate of ion energization integrated over a full wave period $T = 2\pi/\omega$ is zero, because the relative phase shifts $\delta_1 = \delta_2 = -\pi/2$ dictate that the perpendicular ion current is always $-\pi/2$ out of phase with the perpendicular electric field.

As the frequency increases towards the ion cyclotron frequency $\omega/\Omega_i \to 1$, the self-consistent ion response to the electric field fluctuations is calculated by the PLUME Vlasov–Maxwell linear dispersion relation solver[52]. In the case of ion cyclotron damping, the phase of the jth component of the perpendicular ion bulk velocity $U_{\perp j,i}$ increases relative to the jth component of the perpendicular electric field $E_{\perp j}$ into the range $-\pi/2 < \delta_j < 0$, so that the two fields gain an in-phase component; in this case, there is net positive work $\mathbf{j}_{\perp,i} \cdot \mathbf{E}_\perp$ done on the ions by the perpendicular electric field, leading to damping of the ion cyclotron wave.

Data availability

The data used in this research is available to the public via the MMS Science Data Center (https://lasp.colorado.edu/mms/sdc/public/) or from the corresponding author upon request. Source data are provided with this paper (https://doi.org/10.5281/zenodo.13207412).

Code availability

The code used in this research is written in the proprietary Interactive Data Language (IDL) and is available upon request.

References

1. Howes, G. G. A prospectus on kinetic heliophysics. *Phys. Plasmas* **24**, 055907 (2017).
2. National Research Council. *Solar and Space Physics: A Science for a Technological Society* (The National Academies Press, 2013)
3. Mikić, Z., Linker, J. A., Schnack, D. D., Lionello, R. & Tarditi, A. G. Magnetohydrodynamic modeling of the global solar corona. *Phys. Plasmas* **6**, 2217–2224 (1999).

4. Lionello, R., Linker, J. A. & Mikić, Z. Multispectral emission of the sun during the first whole sun month: magnetohydrodynamic simulations. *Astrophys. J.* **690**, 902–912 (2009).
5. Adhikari, L. et al. Turbulence transport modeling and first orbit parker solar probe (PSP) observations. *Astrophys. J. Suppl.* **246**, 38 (2020).
6. Opher, M., Loeb, A., Drake, J. & Toth, G. A small and round heliosphere suggested by magnetohydrodynamic modelling of pick-up ions. *Nat Astron* **4**, 675–683 (2020).
7. Howes, G. G. A prescription for the turbulent heating of astrophysical plasmas. *Mon. Not. Roy. Astron. Soc.* **409**, L104–L108 (2010).
8. Rowan, M. E., Sironi, L. & Narayan, R. Electron and proton heating in transrelativistic magnetic reconnection. *Astrophys. J.* **850**, 29 (2017).
9. Event Horizon Telescope Collaboration. First M87 event horizon telescope results. V. physical origin of the asymmetric ring. *Astrophys. J.* **875**, L5 (2019).
10. Event Horizon Telescope Collaboration. First Sagittarius A* Event Horizon Telescope Results. V. Testing Astrophysical Models of the Galactic Center Black Hole. *Astrophys. J. Lett.* **930**, L16 (2022).
11. Chael, A., Narayan, R. & Johnson, M. D. Two-temperature, magnetically arrested disc simulations of the jet from the supermassive black hole in M87. *Mon. Not. Roy. Astron. Soc.* **486**, 2873–2895 (2019).
12. Landau, L. D. On the vibrations of electronic plasmas. *J. Phys.* **10**, 25 (1946).
13. Chen, C. H. K., Klein, K. G. & Howes, G. G. Evidence for electron Landau damping in space plasma turbulence. *Nat. Commun.* **10**, 740 (2019).
14. Barnes, A. Collisionless damping of hydromagnetic waves. *Phys. Fluids* **9**, 1483–1495 (1966).
15. Isenberg, P. A. & Vasquez, B. J. Perpendicular ion heating by cyclotron resonant dissipation of turbulently generated kinetic Alfvén waves in the solar wind. *Astrophys. J.* **887**, 63 (2019).
16. Chandran, B. D. G. et al. Stochastic heating, differential flow, and the alpha-to-proton temperature ratio in the solar wind. *Astrophys. J.* **776**, 45 (2013).
17. Chandran, B. D. G., Li, B., Rogers, B. N., Quataert, E. & Germaschewski, K. Perpendicular ion heating by low-frequency Alfvén-wave turbulence in the solar wind. *Astrophys. J. Lett.* **720**, 503–515 (2010).
18. Martinović, M. M. et al. The enhancement of proton stochastic heating in the near-sun solar wind. *Astrophys. J. Suppl.* **246**, 30 (2020).
19. Lichko, E. & Egedal, J. Magnetic pumping model for energizing superthermal particles applied to observations of the earth's bow shock. *Nature Commun.* **11**, 2942 (2020).
20. Arzamasskiy, L., Kunz, M. W., Squire, J., Quataert, E. & Schekochihin, A. A. Kinetic turbulence in collisionless high-β plasmas. *Phys. Rev.X* **13**, 021014 (2023).
21. Osman, K. T., Matthaeus, W. H., Greco, A. & Servidio, S. Evidence for inhomogeneous heating in the solar wind. *Astrophys. J. Lett.* **727**, L11 (2011).
22. Zhdankin, V., Uzdensky, D. A. & Boldyrev, S. Temporal intermittency of energy dissipation in magnetohydrodynamic turbulence. *Phys. Rev. Lett.* **114**, 065002 (2015).
23. Mallet, A., Schekochihin, A. A. & Chandran, B. D. G. Disruption of Alfvénic turbulence by magnetic reconnection in a collisionless plasma. *J. Plasma Phys.* **83**, 905830609 (2017).
24. Loureiro, N. F. & Boldyrev, S. Role of magnetic reconnection in magnetohydrodynamic turbulence. *Phys. Rev. Lett.* **118**, 245101 (2017).
25. Kasper, J. C., Lazarus, A. J. & Gary, S. P. Hot solar-wind helium: direct evidence for local heating by Alfvén-cyclotron dissipation. *Phys. Rev. Lett.* **101**, 261103 (2008).
26. Kasper, J. C., Maruca, B. A., Stevens, M. L. & Zaslavsky, A. Sensitive test for ion- cyclotron resonant heating in the solar wind. *Phys. Rev. Lett.* **110**, 091102 (2013).
27. Case, A. W. et al. The solar probe cup on the parker solar probe. *Astrophys. J. Suppl.* **246**, 43 (2020).
28. Fox, N. J. et al. The solar probe plus mission: humanity's first visit to our star. *Space Sci. Rev.* **204**, 7–48 (2016).
29. Kasper, J. C. et al. Solar wind electrons alphas and protons (SWEAP) investigation: design of the solar wind and coronal plasma instrument suite for solar probe plus. *Space Sci. Rev.* **204**, 131–186 (2016).
30. Vech, D. et al. Wave-particle energy transfer directly observed in an ion cyclotron wave. *Astron. Astrophys.* **650**, A10 (2021).
31. Bowen, T. A. et al. In situ signature of cyclotron resonant heating in the solar wind. *Phys. Rev. Lett.* **129**, 165101 (2022).
32. Klein, K. G. & Howes, G. G. Measuring collisionless damping in heliospheric plasmas using field-particle correlations. *Astrophys. J. Lett.* **826**, L30 (2016).
33. Howes, G. G., Klein, K. G. & Li, T. C. Diagnosing collisionless energy transfer using field- particle correlations: Vlasov-Poisson plasmas. *J. Plasma Phys.* **83**, 705830102 (2017).
34. Klein, K. G., Howes, G. G. & Tenbarge, J. M. Diagnosing collisionless energy transfer using field-particle correlations: gyrokinetic turbulence. *J. Plasma Phys.* **83**, 535830401 (2017).
35. Klein, K. G., Howes, G. G., TenBarge, J. M. & Valentini, F. Diagnosing collisionless energy transfer using field-particle correlations: Alfvén-ion cyclotron turbulence. *J. Plasma Phys.* **86**, 905860402 (2020).
36. Burch, J. L., Moore, T. E., Torbert, R. B. & Giles, B. L. Magnetospheric multiscale overview and science objectives. *Space Sci. Rev.* **199**, 5–21 (2016).
37. Afshari, A. S., Howes, G. G., Kletzing, C. A., Hartley, D. P. & Boardsen, S. A. The importance of electron landau damping for the dissipation of turbulent energy in terrestrial magnetosheath plasma. *J. Geophys. Res.: Space Phys.* **126**, e29578 (2021).
38. Huang, S. Y., Hadid, L. Z., Sahraoui, F., Yuan, Z. G. & Deng, X. H. On the existence of the kolmogorov inertial range in the terrestrial magnetosheath turbulence. *Astrophys. J. Lett.* **836**, L10 (2017).
39. Russell, C. T. et al. The magnetospheric multiscale magnetometers. *Space Sci. Rev.* **199**, 189–256 (2016).
40. Ergun, R. E. et al. The axial double probe and fields signal processing for the MMS mission. *Space Sci. Rev.* **199**, 167–188 (2016).
41. Lindqvist, P. A. et al. The spin-plane double probe electric field instrument for MMS. *Space Sci. Rev.* **199**, 137–165 (2016).
42. Pollock, C. et al. Fast Ppasma investigation for magnetospheric multiscale. *Space Sci. Rev.* **199**, 331–406 (2016).
43. Lion, S., Alexandrova, O. & Zaslavsky, A. Coherent events and spectral shape at ion kinetic scales in the fast solar wind turbulence. *Astrophys. J.* **824**, 47 (2016).
44. Bowen, T. A. et al. Ion-scale electromagnetic waves in the inner heliosphere. *Astrophys. J. Suppl.* **246**, 66 (2020).
45. Goldreich, P. & Sridhar, S. Toward a theory of interstellar turbulence II. strong Alfvénic turbulence. *Astrophys. J.* **438**, 763–775 (1995).
46. Schekochihin, A. A. et al. Astrophysical gyrokinetics: kinetic and fluid turbulent cascades in magnetized weakly collisional plasmas. *Astrophys. J. Suppl.* **182**, 310–377 (2009).
47. Gary, S. P., Montgomery, M. D., Feldman, W. C. & Forslund, D. W. Proton temperature anisotropy instabilities in the solar wind. *J. Geophys. Res.* **81**, 1241–1246 (1967).
48. Squire, J. et al. High-frequency heating of the solar wind triggered by low-frequency turbulence. *Nature Astron.* **6**, 715–723 (2022).
49. Arzamasskiy, L., Kunz, M. W., Chandran, B. D. G. & Quataert, E. Hybrid-kinetic simulations of ion heating in Alfvénic turbulence. *Astrophys. J.* **879**, 53 (2019).

50. Klein, K. G. & Chandran, B. D. G. Evolution of the proton velocity distribution due to stochastic heating in the near-sun solar wind. *Astrophys. J.* **820**, 47 (2016).
51. Cerri, S. S., Arzamasskiy, L. & Kunz, M. W. On stochastic heating and its phase-space signatures in low-beta kinetic turbulence. *Astrophys. J.* **916**, 120 (2021).
52. Klein, K. G. & Howes, G. G. Predicted impacts of proton temperature anisotropy on solar wind turbulence. *Phys. Plasmas* **22**, 032903 (2015).
53. Verscharen, D. et al. ALPS: the arbitrary linear plasma solver. *J. Plasma Phys.* **84**, 905840403 (2018).
54. Johnson, J. R. & Cheng, C. Z. Stochastic ion heating at the magnetopause due to kineticAlfvén waves. *Geophys. Res. Lett.* **28**, 4421–4424 (2001).
55. Horvath, S. A., Howes, G. G. & McCubbin, A. J. Electron Landau damping of kinetic Alfvén waves in simulated magnetosheath turbulence. *Phys. Plasmas* **27**, 102901 (2020).
56. Howes, G. G. et al. A model of turbulence in magnetized plasmas: implications for the dissipation range in the solar wind. *J. Geophys. Res.: Space Phys.* **113**, A05103 (2008).
57. Howes, G. G., Tenbarge, J. M. & Dorland, W. A weakened cascade model for turbulence in astrophysical plasmas. *Phys. Plasmas* **18**, 102305–102305 (2011).
58. Horvath, S. A., Howes, G. G. & McCubbin, A. J. Observing particle energization above the Nyquist frequency: an application of the field-particle correlation technique. *Phys. Plasmas* **29**, 062901 (2022).
59. Bourouaine, S. & Chandran, B. D. G. Observational test of stochastic heating in Low-β fast-solar-wind streams. *Astron. J.* **774**, 96 (2013).
60. Howes, G. G., McCubbin, A. J. & Klein, K. G. Spatially localized particle energization by Landau damping in current sheets produced by strong Alfvén wave collisions. *J. Plasma Phys.* **84**, 905840105 (2018).
61. Juno, J. et al. A field-particle correlation analysis of a perpendicular magnetized collisionless shock. *J. Plasma Phys.* **87**, 905870316 (2021).
62. Juno, J. et al. Phase-space energization of ions in oblique shocks. *Astrophys. J.* **944**, 15 (2023).
63. Schroeder, J. W. R. et al. Laboratory measurements of the physics of auroral electron acceleration by Alfvén waves. *Nature Commun.* **12**, 3103 (2021).
64. McCubbin, A. J., Howes, G. G. & TenBarge, J. M. Characterizing velocity-space signatures of electron energization in large-guide-field collisionless magnetic reconnection. *Phys. Plasmas* **29**, 052105 (2022).
65. Torbert, R. B. et al. The FIELDS instrument suite on MMS: scientific objectives, measurements, and data products. *Space Sci. Rev.* **199**, 105–135 (2016).
66. Chen, C. H. K., Bale, S. D., Salem, C. & Mozer, F. S. Frame dependence of the electric field spectrum of solar wind turbulence. *Astrophys. J. Lett.* **737**, L41 (2011).
67. Howes, G. G., Klein, K. G. & TenBarge, J. M. Validity of the Taylor hypothesis for linear kinetic waves in the weakly collisional solar wind. *Astrophys. J. Lett.* **789**, 106 (2014).
68. Montag, P. & Howes, G. G. A field-particle correlation analysis of magnetic pumping. *Phys. Plasmas* **29**, 032901 (2022).

Acknowledgements

K.G.K. was supported by NASA Grant 80NSSC19K0912 and 80NSSC20K0521. The authors would like to thank the MMS instrument teams for their assiduous dedication in calibrating their data.

Author contributions

A.S.A. performed the scientific analysis and wrote the initial manuscript text. G.G.H. contributed to the development of the analysis method, interpretation of the results, modeling of the results, and the manuscript text. J.R.S. provided insight and input into the analysis of the data. K.G.K. contributed to the development of the analysis method, interpretation of the results, numerical simulations, and linear wave analysis. D.M. contributed to the data analysis. M.M.M. contributed the wave analysis. S.A.B. provided details for the data processing and wave analysis. C.R.B. and R.H. contributed to the development of the model. D.P.H. contributed to the data analysis. C.A.K. assisted with the interpretation of the results.

Competing interests

The authors declare no competing interests.

Additional information

Supplementary information The online version contains supplementary material available at https://doi.org/10.1038/s41467-024-52125-8.

Correspondence and requests for materials should be addressed to A. S. Afshari.

Peer review information *Nature Communications* thanks Alfred Mallet, and the other, anonymous, reviewers for their contribution to the peer review of this work. A peer review file is available.